



OPEN

Ultra-fast germanium photodiode with 3-dB bandwidth of 265 GHz

S. Lischke¹✉, A. Peczek¹, J. S. Morgan¹, K. Sun³, D. Steckler¹, Y. Yamamoto¹, F. Korndörfer¹, C. Mai¹, S. Marschmeyer¹, M. Fraschke¹, A. Krüger¹, A. Beling³ and L. Zimmermann^{1,4}

On a scalable silicon technology platform, we demonstrate photodetectors matching or even surpassing state-of-the-art III-V devices. As key components in high-speed optoelectronics, photodetectors with bandwidths greater than 100 GHz have been a topic of intense research for several decades. Solely InP-based detectors could satisfy the highest performance specifications. Devices based on other materials, such as germanium-on-silicon devices, used to lag behind in speed, but enabled complex photonic integrated circuits and co-integration with silicon electronics. Here we demonstrate waveguide-coupled germanium photodiodes with optoelectrical 3-dB bandwidths of 265 GHz and 240 GHz at a photocurrent of 1 mA. This outstanding performance is achieved by a novel device concept in which a germanium fin is sandwiched between complementary in situ-doped silicon layers. Our photodetectors show internal responsivities of 0.3 A W⁻¹ (265 GHz) and 0.45 A W⁻¹ (240 GHz) at a wavelength of 1,550 nm. The internal bandwidth-efficiency product of the latter device is 86 GHz. Low dark currents of 100–200 nA are obtained from these ultra-fast photodetectors.

Integrated photonics has enabled the digital communication age, which relies on optical networks at all levels to transport data at very high speed and low cost. Large-scale data centres require highly integrated cost-efficient optical communication solutions, because data-centre interconnects are becoming one of the main cost factors. The technical and economic necessities associated with optical interconnects have fostered the development and rapid maturation of two integrated photonics technology platforms for use in the 1,300–1,600 nm range that is prevalent today. The platforms are conventionally denominated by their material base: (1) silicon photonics and (2) indium phosphide (InP)-based integrated photonics. The importance of the two platforms goes way beyond optoelectronic transceivers and optical communications. Both silicon photonics and InP-based photonics find applications in terahertz generation and sensing, high-speed signal processing and potentially neuromorphic computing. Although silicon photonics enjoys some clear advantages over InP integrated photonics, such as its scalability up to 300-mm wafers and wafer-level co-integration with high-speed electronics, the ultimate and benchmark photodetector performances are achieved with InP^{1,2}. InP-based waveguide-coupled photodiodes, even several years ago, had already demonstrated 3-dB bandwidths ($f_{3\text{-dB}}$) of 170 GHz and responsivities of 0.27 A W⁻¹ (ref. ³). By contrast, germanium photodiodes, which are available on the major silicon photonics platforms, typically show bandwidths in the range of 50–70 GHz (refs. ^{4–7}). Beyond these, the demonstration of a germanium photodiode with $f_{3\text{-dB}} \approx 120$ GHz and rather high dark current stands out, with some uncertainty regarding the bandwidth due to measurement limitations⁸.

In this Article we demonstrate a genuine silicon photonic photodetector approaching the ultimate performance in terms of optoelectronic bandwidth and responsivity—a silicon waveguide-coupled p-i-n photodiode based on epitaxially grown germanium. Our germanium photodiode shows a bandwidth in excess of 260 GHz

at a photocurrent of 1 mA. This device outperforms all other silicon integrated photodetector approaches demonstrated so far by showing a very high bandwidth and substantially high responsivity, while exhibiting low dark current. In terms of the optoelectronic bandwidth only, even the fastest waveguide-coupled III-V photodetectors are outperformed by these germanium photodiodes. Zero-bias 3-dB bandwidths of >65 GHz are achieved, as have already been demonstrated for III-V photodetectors⁹, but not for germanium-based photodiodes until now.

Our work proves that the conventional silicon technology available for standard 200-mm or 300-mm silicon substrates can match or even outperform InP technology in terms of high-speed waveguide-coupled photodetector performance, without the need to resort to more cumbersome III-V material transfer approaches.

Results

Fabrication. In this Article we demonstrate a novel approach that has similarities to the basic fabrication flow described in ref. ¹⁰, in which we demonstrated germanium photodiodes with bandwidths of 110 GHz. However, there are some important differences. With our unique approach, we deviate from the conventional germanium-waveguide integrated design paradigm by developing a novel biconcave germanium fin shape, analogous to the well-known FinFET transistors. This biconcave form of our vertically aligned germanium fin allows the narrowest germanium width to be in the centre of the waveguide, where the optical intensity is supposed to be highest, leading to the shortest transit times for photocarriers. Our approach is based on an initially few-micrometre-wide germanium body with a height of ~400 nm, which is thick enough to ensure sufficiently good crystalline quality. This is a distinctive feature compared to vertical drift field diodes, where the epitaxial growth of thin germanium layers (<100 nm) with low defect density is very difficult, and thus the fabrication of photodiodes with reasonably low dark currents is quite challenging¹¹.

¹IHP – Leibniz-Institut für innovative Mikroelektronik, Frankfurt (Oder), Germany. ²IHP Solutions GmbH, Frankfurt (Oder), Germany. ³Department of Electrical and Computer Engineering, University of Virginia, Charlottesville, VA, USA. ⁴Technische Universität Berlin, Institut für HF- und HL-Systemtechnologien, Berlin, Germany. ✉e-mail: lischke@ihp-microelectronics.com

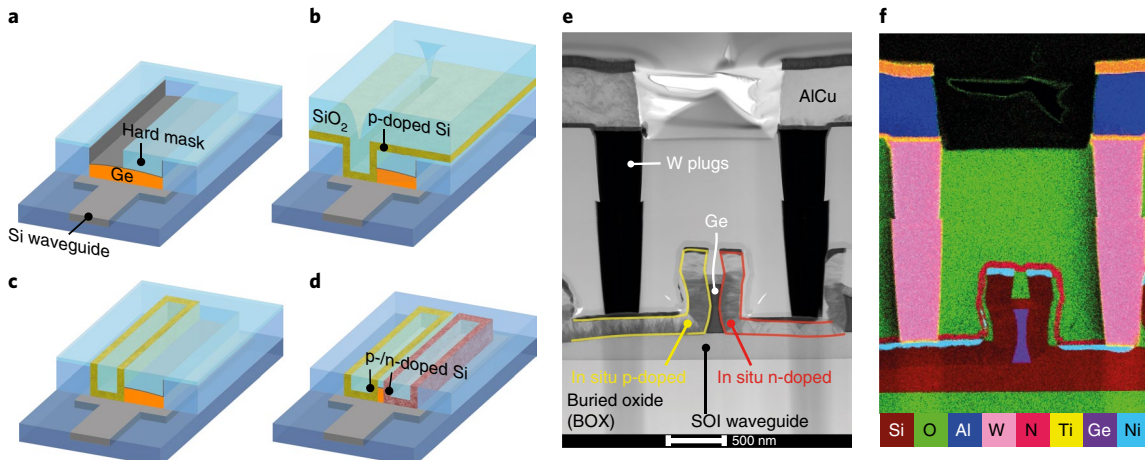


Fig. 1 | Process flow for the germanium-fin photodetector design and cross-sectional images of a germanium photodiode. **a–d**, Illustration of the process flow for the germanium-fin photodetector design. A cut through the structure provides a cross-sectional image for each stage. **a**, On top of a selectively grown germanium body on an SOI waveguide, on one side, a SiO_2 hard mask is deposited and patterned. **b**, Dry etch of germanium via the hard mask and subsequent epitaxial deposition of an in situ p-doped silicon layer is followed by overfill with SiO_2 . **c**, CMP is performed to restore a planar surface and to remove the p-doped Si layer in the outer regions. The hard-mask SiO_2 layer is patterned on the opposite side, followed by a germanium dry etch, in situ n-doped Si epitaxy, plus the planarization steps, as before. **d**, Finally, an (undoped) germanium fin is realized, which is sandwiched between two complementary in situ-doped silicon layers, such that a lateral Si–Ge–Si p-i-n diode is formed, without the need for ion implantation. More details on the fabrication are provided in the Methods. **e**, Cross-sectional image, obtained by STEM, of a germanium photodiode (termed Ge100_10) that features in situ-doped (different colours for p- and n-doping) silicon contact regions (**f**) and an EDX image of the same device. The nominal width is 100 nm, while at the narrowest point the germanium fin is only ~60 nm wide. Both cross-sections are cut perpendicular to the direction of light incidence. Electrical contacts to the photodiode are realized with nickel silicide and a state-of-the-art tungsten contact module (two levels), up to the first metal layer (AlCu).

We make use of in situ-doped silicon layers, which allows us to entirely waive ion implantation and thus reduce unintended doping of the germanium. This is very beneficial for the high-speed capability of the photodiodes, as the negative impact of minority-carrier diffusion on the high-speed performance of the detectors is efficiently suppressed. Compared to ref. ¹⁰, we have entirely redesigned the process for the in situ n-doped silicon layer, as described in the Methods.

The narrow germanium fin is realized by sequential patterning and is ultimately sandwiched between two complementary in situ-doped silicon layers. Admittedly, this approach depends on the accuracy of the overlaying of lithography masks relative to each other and precise adjustment of the critical dimensions, which are very well controlled and sufficiently sharp. In the present experiments, the overlay and critical dimension accuracies were typically in the range of <10 nm and ~30 nm, respectively. This accuracy was confirmed on several wafers in follow-up lots, so we believe that our approach is potentially suited for the reliable fabrication of germanium-fin photodiodes with feature sizes of 100 nm or less. Fabrication of the novel germanium photodiodes is entirely conducted on IHP's 8-inch BiCMOS pilot line facilities. We utilize 8-inch silicon-on-insulator (SOI) substrate wafers. A schematic of the fabrication flow is presented in Fig. 1a–d.

The in situ-doped silicon layers beside the germanium fin also form laterally oriented offshoots, which, after formation of a silicide layer, enable low-ohmic contacts to access the diode. Tungsten contact plugs are positioned on these silicided silicon offshoots at a safe distance from the optical mode at the same time. Electrical contacting is realized by one layer of AlCu. Additional metal layers that are commonly used have been omitted to save manufacturing time. A cross-sectional image of the device, including the contacts and the first metal layer, is provided in Fig. 1e. We equipped the devices with ground–signal–ground (GSG) pads with pitches of 100 μm and 150 μm to match the different requirements of the respective radiofrequency probes in the lightwave component analyser- and heterodyne measurement set-ups.

Device characterization. Compared to the devices from our previous work¹⁰ or any other state-of-the-art germanium photodiodes^{4,7,12–15}, our new photodiodes feature germanium regions with drastically narrowed lateral sizes, as low as ~60 nm. This leads to even higher electric-fields and shorter photocarrier drift times (carrier velocity saturation has long been reached at –2 V for a width of 600 nm or smaller, assuming perfectly vertical sidewalls).

To study the final device dimensions and material quality with high precision and in great detail, scanning transmission electron microscopy (STEM) and energy-dispersive X-ray spectroscopy (EDX) analyses were performed. Cross-sectional images obtained with these techniques are presented in Fig. 1e,f, respectively, based on a lamella created by a focused ion beam. With its biconcave form, the width of the germanium fin at its narrowest point (~60 nm in the centre) is much smaller than at its broadest point (~140 nm at the bottom). We therefore define a nominal device width of 100 nm for the fin, which is the mean of these values.

Compared to the diodes with $f_{3-\text{dB}} \geq 110$ GHz described in ref. ¹⁰, this is a reduction in width of ~67%. With both silicon layers on the sides of the germanium fin, the diodes have total lateral widths of a few hundred nanometres. The height of the germanium fin is ~400 nm and the devices presented in this work are 10 μm in length, long enough to ensure sufficient absorption at a wavelength of 1,550 nm. In accordance with the naming scheme already used in ref. ¹⁰, the device with a nominal germanium width of 100 nm and length of 10 μm is termed ‘Ge100_10’ in the following. To clearly distinguish the different devices from this work and ref. ¹⁰ (in which all diodes were 20 μm long), here we also include the device lengths in the labelling. A slightly broader device with nominal width of 150 nm (width of ~110 nm at the narrowest point) is accordingly named Ge150_10.

From the STEM images, it becomes obvious that the vertical sidewalls of the germanium fin are fairly steep, guaranteeing a homogeneous electric field across the light-sensitive germanium, which is important for efficient collection of photogenerated carriers. Sidewall spacers at the vertical sidewalls along the germanium

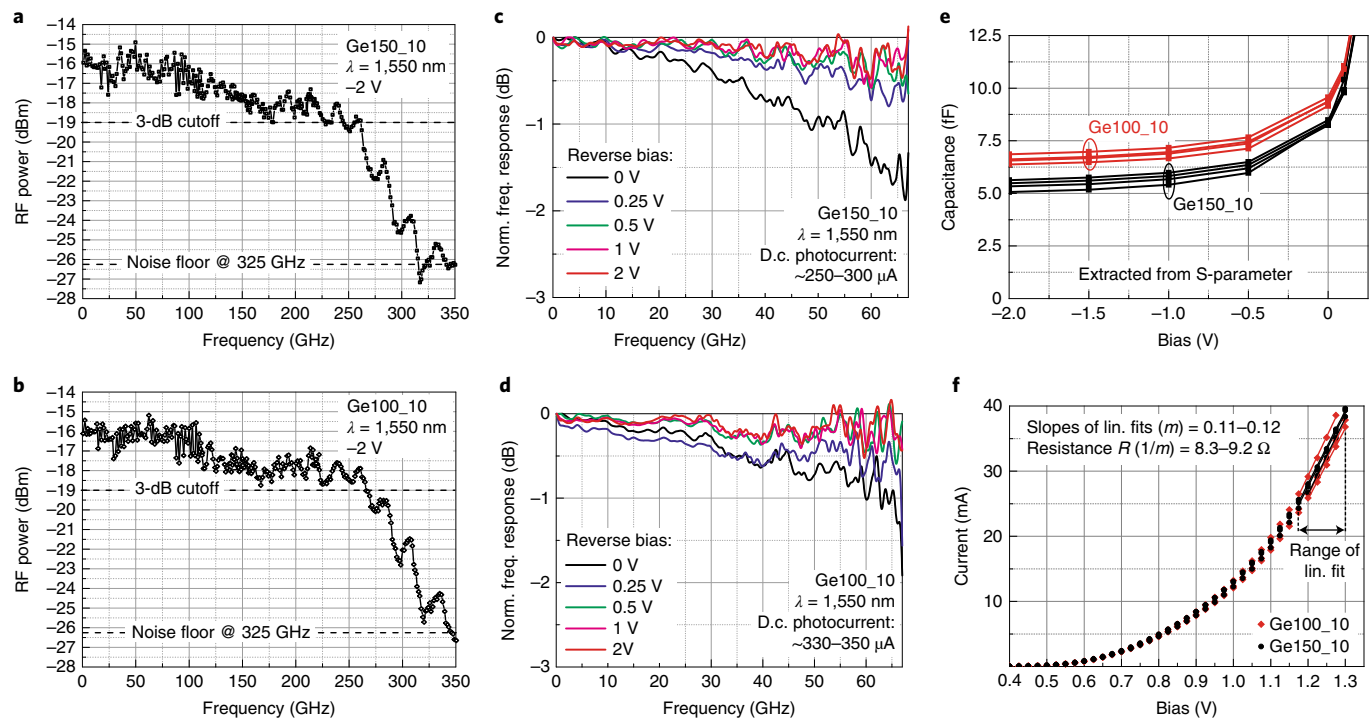


Fig. 2 | Small signal optoelectronic frequency response and low-frequency electric device characterization. **a,b**, Frequency responses from a heterodyne measurement set-up for the Ge150_10 (**a**) and Ge100_10 (**b**) diodes, each measured at a d.c. photocurrent of 1 mA. Measurements were performed at a reverse bias of 2 V on diodes from the same chip and wafer. Diodes with nominal germanium widths of 150 nm and 100 nm yield 3-dB bandwidths of 240 GHz and 265 GHz, respectively. RF, radiofrequency. **c,d**, Frequency responses measured with a 67-GHz LCA under different bias conditions for the Ge150_10 (**c**) and Ge100_10 (**d**) diodes. Both diodes show 1-dB bandwidths in excess of 70 GHz, even under very small reverse bias, in good agreement with results from the heterodyne measurements. **e,f**, Bias-dependent capacitances for both diodes from four chips from the same wafer (**e**) and series resistances derived from forward bias I-V curves (**f**) are used for estimation of cutoff frequencies.

fin (shown in Fig. 1f) prohibit the formation of silicide in close proximity to the germanium, preventing additional optical losses. At the same time, these spacers adjust the distance between the silicide on the lateral silicon offshoots and the germanium fin. The lower parts of the two-stage tungsten plug contact scheme are located on the nickel silicide on top of the lateral silicon offshoots, where the etch process for the plugs has stopped precisely on top of the silicide, which is crucial for low-ohmic contact resistances.

Optoelectrical high-speed characterization. For estimation of the high-speed optoelectrical properties we used two different set-ups, each with its own individual capabilities and limitations. Calibrated heterodyne measurements up to 325 GHz were performed so the measurement set-up did not limit investigations of the 3-dB bandwidths. On a second set-up, measurements were performed with a 67-GHz lightwave component analyser (LCA). On the heterodyne set-up, characterization of photodiodes is possible at the chip level, whereas measurements are performed separately for the different frequency bands (d.c. to 110 GHz, 110–170 GHz, 140–220 GHz and 220–325 GHz) due to the requirement for specific probes and power meter transitions for each of the radiofrequency bands. Schematic sketches of the heterodyne measurement set-ups are provided in Supplementary Figs. 2 and 3.

After screening various designs on the 67-GHz LCA-based set-up, heterodyne measurements were taken on selected photodiodes up to 350 GHz. The results for these are presented in Fig. 2a,b, which shows the frequency response of two photodiodes with different germanium widths. The germanium Ge100_10 photodetector achieves a 3-dB bandwidth of 265 GHz at a d.c. photocurrent of 1.0 mA, which is an improvement of a factor of ~2.4 compared to ref. ¹⁰.

This device even outperforms the best waveguide-coupled InP photodiodes in terms of their high-speed performance. A photodiode with a slightly broader germanium fin, device Ge150_10, shows a 3-dB bandwidth of 240 GHz at the same d.c. photocurrent of 1.0 mA.

Unlike the heterodyne measurement, with the 67-GHz LCA, wafer-level investigations on a semi-automated wafer probe are possible. Here, the frequency response is determined from optoelectrical S-parameter (scattering parameter) measurements. Limited by the bandwidth of the LCA, a complete assessment of the frequency response and thus the 3-dB bandwidths was not possible for our novel germanium photodiodes. However, this set-up allows for a more extensive investigation, such as the screening of multiple device layouts and various bias and optical power conditions for numerous chips. A schematic sketch of the measurement set-up with the 67-GHz LCA is provided in Supplementary Fig. 4.

Figure 2c,d presents normalized frequency response curves under various bias conditions for the Ge150_10 and Ge100_10 photodiodes, respectively. Both devices show only small reverse bias dependencies at d.c. photocurrents of 250–350 μA and yield 3-dB bandwidths that are already certainly higher than 70 GHz at zero bias, which is a notable improvement over the results in ref. ¹⁰. However, for the Ge150_10 photodiode, the frequency response changes are most noticeable between zero bias and −0.25 V, which indicates that the germanium might not be fully depleted at small or zero bias. This could mean that there remains a certain amount of doping in the germanium region. We suspect that there might be a doping gradient near the in situ-doped silicon layer(s), for example, as a result of dopant diffusion, despite the abandonment of ion implantation. Capacitance–voltage characteristics, extracted

Table 1 | Estimation of $f_{3\text{-dB}}$ by taking carrier drift time and RC time constant into account

Values at -2 V	Ge100_10	Ge150_10
Nominal width (nm)	100	150
Effective width (nm)	~80	~130
Depletion width, w_D (nm)	~90–100	~115–120
Resistance, R (Ω)	59	59
Capacitance, C (fF)	6.5	5.5
Calculated f_{RC} (GHz)	415	490
Calculated f_{TT} (GHz)	358	220
Calculated $f_{3\text{-dB}}$ (GHz)	271	201
Measured $f_{3\text{-dB}}$ (GHz)	265	240
Internal responsivity (A W^{-1})	0.3	0.45
Internal quantum efficiency	0.24	0.36
External responsivity (A W^{-1})	0.12	0.2
External quantum efficiency	0.1	0.16
Bandwidth-efficiency product (GHz)	63	86

Resistance values include series resistances and the $50\text{-}\Omega$ load from the measurement set-up. Capacitances were extracted from S-parameter measurements. The depletion widths are calculated from the capacitances, under the assumption of perfectly vertical sidewalls and parasitic capacitances from the protruding vertical silicon offshoots. We assume that the biggest fraction of the light would be absorbed nearby and in the centre, where the widths are certainly smaller than the nominal widths, which is why we define an effective width for the estimation of f_{TT} . Responsivities have solely been estimated at a wavelength of 1,550 nm. For the bandwidth-efficiency products we refer to the internal responsivities and quantum efficiencies as the external values are mainly dominated by the grating coupler efficiencies and not by the photodiodes themselves.

from S-parameter measurements, help us to investigate this assertion (Fig. 2e). Series resistances were derived from forward-biased I-V curves measured on three representative chips for both diodes (Fig. 2f). These, together with the capacitances, form the basis for estimation of the cutoff frequency.

As shown in Fig. 2e, for the narrowest device, Ge100_10, the capacitance drops from $\sim 9.5\text{ fF}$ at zero bias to $\sim 6.5\text{ fF}$ at -2 V . Under a parasitic capacitance of $\sim 0.6\text{ fF}$ resulting from the protruding vertical silicon offshoots, these values correspond to a change in the depletion widths from $\sim 65\text{ nm}$ to $\sim 90\text{--}100\text{ nm}$ (400-nm-high and $10\text{-}\mu\text{m}$ -long germanium), which matches very well the width estimated by STEM. For simplicity we assume perfectly parallel sidewalls, using $w_D = \epsilon_0 \epsilon_r A/C$, where w_D is the depletion width, ϵ_0 is the vacuum permittivity, ϵ_r is the relative permittivity, A is the area and C is the extracted capacitance. For the wider device, Ge150_10, the capacitance of $\sim 5.5\text{ fF}$ at -2 V corresponds to a depletion width of $\sim 115\text{--}120\text{ nm}$ (we considered a parasitic capacitance of $\sim 0.4\text{ fF}$). Table 1 summarizes the cutoff frequencies f_{TT} (by transit time, under the assumption of a saturation drift velocity of $0.65 \times 10^7\text{ cm s}^{-1}$ for bulk germanium) and f_{RC} (capacitance C and resistance R , with $f_{RC} = 1/(2\pi RC)$). Resistance R includes the series resistance from I-V curves plus the $50\text{-}\Omega$ load of the measurement set-up, and capacitance C was extracted from small signal measurements. Finally, considering the photocarrier transit time and RC time constant only, the $f_{3\text{-dB}}$ bandwidths for both diodes were calculated according to ref. ¹⁶. For photodiode Ge100_10, the calculated and measured 3-dB bandwidths match very well. As we solely consider RC and transit time constants in our calculations, we assume that minority-carrier diffusion plays no further role in the high-speed performance, at least not at a bias of -2 V . For the wider photodiode, Ge150_10, there remains some mismatch, probably caused by the relatively low f_{TT} of 220 GHz that we derived from the carrier transit time over a distance of 130 nm. However, we have to consider that

the germanium thickness varies in a range of $\sim 10\%$ over the length of the diode, which not only has an impact on the estimated depletion width but also affects the actual width of the germanium fin due to the biconcave form that is created during the etch process. Uncertainties in the range of $\sim 10\text{--}20\%$ in the germanium fin width seem thoroughly plausible. For example, a reduction in the width of 10% already leads to $\sim 24\text{-GHz}$ higher f_{TT} and almost a 20-GHz increase in $f_{3\text{-dB}}$.

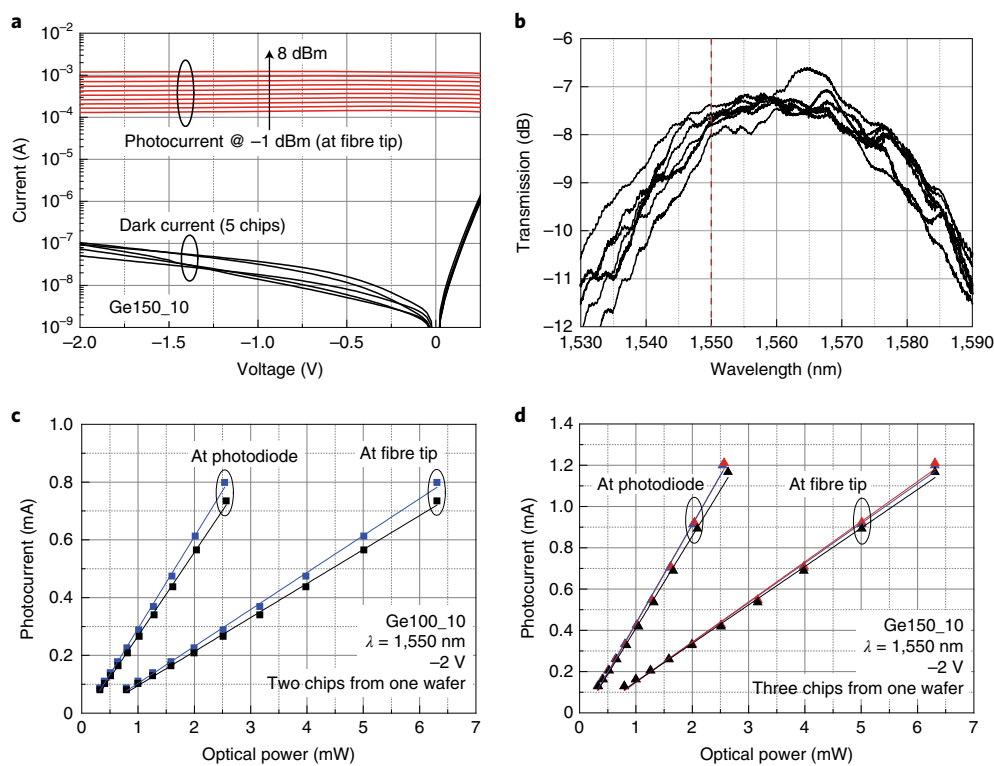
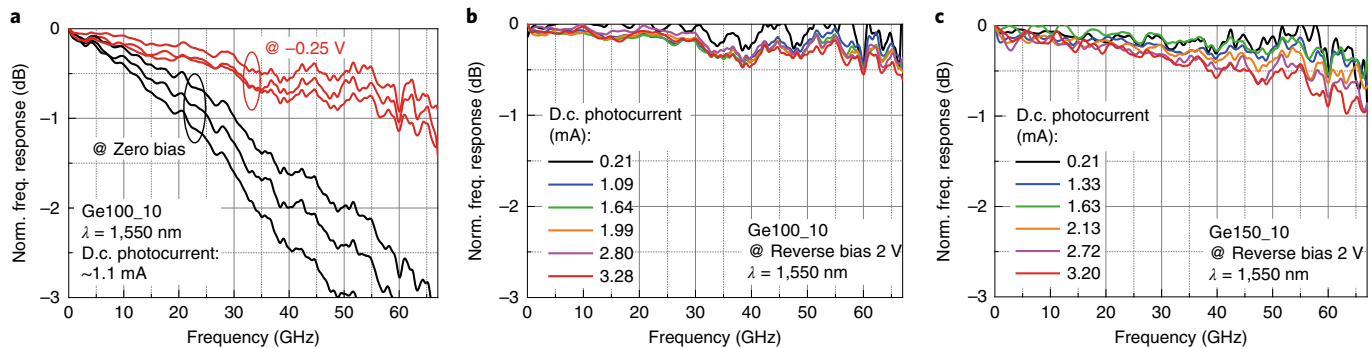
At increased optical input power (d.c. photocurrents of $\sim 1.1\text{ mA}$), a small decrease in the frequency response curves at zero bias can be seen, as shown in Fig. 3a (for Ge100_10 measured on three chips). Under small reverse bias (-0.25 V), this effect is already almost completely compensated as 1-dB bandwidths of 60 GHz or above are restored. Frequency response curves under a reverse bias of 2 V for various optical input power conditions are shown in Fig. 3b,c for the two device types measured at the same chips of one wafer. It can be seen that the 1-dB bandwidths remain above 67 GHz, even for high d.c. photocurrents of 3.2 mA . This robustness against increased photocurrents is a huge improvement compared to our previous results¹⁰ where, with a current of $\sim 3\text{ mA}$, the 3-dB bandwidth had already dropped to $\sim 60\text{ GHz}$. Owing to the deployed coupling scheme and the available erbium-doped fibre amplifier (EDFA) on our 67-GHz LCA set-up, investigations with photocurrents larger than 3.2 mA were not possible, but are planned for the future.

Optical performance. Photocurrents and dark currents, measured at various optical input powers (at fibre tip) and bias voltages are shown in Fig. 4a for device Ge150_10. The dark currents (in the range of 100 nA) at room temperature are three to four orders of magnitude lower than the photocurrents (in the range of $0.1\text{--}1.2\text{ mA}$). To estimate the internal responsivity, the losses of the grating coupler and the in-coupling waveguide have to be considered. Transmission spectra of a dedicated test structure (two of the grating couplers with a very short waveguide (2 mm), such that the waveguide propagation losses are negligible) are shown in Fig. 4b. Obviously, the maxima are not perfectly positioned at 1,550 nm, so lower loss can be expected at this wavelength once the grating coupler is fully optimized. At 1,550-nm wavelength, the loss of one single grating coupler is $\sim 3.9\text{ dB}$ (7.8-dB total loss for the test structure), which equals a coupling efficiency of $\sim 40\%$ (more details are provided in the Methods). Plots of the photocurrent versus optical power are provided in Fig. 4c,d, each measured at a bias of -2 V . It is worth noting that no saturation is seen up to high photocurrents of 2.5 mA (at 8 dBm at the fibre tip, equal to 6.3 mW). From the slope of the linear regression of the measured data points, external (at the fibre tip) and internal (at the photodiode) responsivities are determined.

A summary of the internal and external responsivities and quantum efficiencies is available in Table 1. Given the ultra-high bandwidth and this substantially high internal responsivity, photodiode Ge150_10 shows a bandwidth-efficiency product of 86 GHz.

Discussion

Our novel photodetectors combine ultra-high bandwidths of 265 GHz and 240 GHz, determined by heterodyne measurements at a photocurrent of 1.0 mA at -2 V , with low dark currents and substantially high responsivities of 0.3 A W^{-1} and 0.45 A W^{-1} . In terms of speed, these devices even outperform the hitherto most sophisticated waveguide-coupled InP-based photodetectors. Zero-bias bandwidths of $>65\text{ GHz}$ are achieved for germanium photodetectors, while for InP-based devices, such high zero-bias bandwidth has already been demonstrated⁹. Up to a d.c. photocurrent of 3.2 mA , which is the maximum d.c. photocurrent that could be reached with the available EDFA and the one-dimensional (1D) grating couplers, our novel devices show 1-dB bandwidths of $>67\text{ GHz}$. A current-carrying capacity beyond 3 mA of photocurrent is part of ongoing investigations.



The room-temperature dark currents are below 200 nA at a bias of -2 V for both Ge100_10 and Ge150_10 diodes, as shown in Fig. 4a for photodiode Ge150_10. At 85°C , the dark currents increase noticeably, but remain safely below 1 μA , so implementation of our novel ultra-fast germanium photodiodes in actual photonic integrated circuits (for example, in data-centre applications) would certainly be feasible. More details on dark current, including results up to 125°C , are provided in Supplementary Fig. 2.

Equipping these ultra-fast diodes with inverse tapers could significantly boost their external responsivities. Coupling losses of 1.5 dB, which have already been demonstrated¹⁷, in combination

with device Ge150_10 would yield a bandwidth-efficiency product of $\sim 60\text{ GHz}$. It is thus feasible that the good external responsivity-based bandwidth-efficiency product of 55 GHz (ref. ¹⁸) would then be in reach.

Key parameters of the various state-of-the-art waveguide-coupled as well as side-illuminated detectors reported in the literature are compared in Table 2. For fair benchmarking of the photodiode performances independently from the coupling approach, we compare bandwidth-efficiency products based on external (InP) as well as internal (for silicon photonics) responsivities and thus quantum efficiencies. In fact, for InP-based detectors, top illumination

Table 2 | Overview of state-of-the-art waveguide-coupled and side-illuminated waveguide photodetectors

	Ref. 18	Ref. 20	Ref. 3	Ref. 21	Ref. 22	Ref. 8	Ref. 5	Ref. 15	Ref. 10	This work	
										Ge150_10	Ge100_10
Material	InP	InP	InP	InP	Graphene	Ge	Ge	Ge	Ge	Ge	Ge
3-dB optoelectronic bandwidth (GHz)	110	145	170	130	≥110 (-1V)	120 (-2 V)	67 (-1V)	67 (-1)	≥110	240	265
Bandwidth-efficiency product (GHz)	55 (ext.)	41 (ext.)	37 (ext.)	47 (ext.)	44 (ext.)	-	-	40 (int.)	24/56 (ext./int.)	38/86 (ext./int.)	25/63 (ext./int.)
Internal resp. (A W ⁻¹)	NA	NA	NA	NA	NA	0.8	NA	0.74	0.64	0.45	0.3
External resp. (A W ⁻¹)	0.63	0.35	0.27	0.45	0.5 (-0.4 V)	NA	NA	NA	0.27	0.2	0.12
Dark current (nA)	NA	NA	NA	2 (-5 V)	4,000 (-0.4 V)	4,000 (-1 V)	20 (-1V)	<4 (-1V)	~300 (-2 V)	≤100 (-2 V)	≤200 (-2 V)

Compared are the 3-dB bandwidths, internal (int.) and external (ext.) responsivities (resp.) as well as dark currents. All results were determined at C-band/1,550 nm, except for ref. ⁵ for which only O-band results are available (and are not included here). Values in parentheses indicate the respective bias conditions (NA indicates values that are not available in the original publication). For fair benchmarking of photodiode performances we compare bandwidth-efficiency products based on external (InP) as well as internal (for silicon photonics) responsivities due to the fact that for InP, fibre-to-waveguide coupling is usually performed. By contrast, in silicon-based platforms, grating couplers are most commonly used, whose efficiencies dominate the external quantum efficiency.

and fibre-to-waveguide coupling by cleaved facets are common, whereas for silicon-based platforms, grating couplers are commonly deployed to couple to nanowaveguides, as in our case. Their coupling efficiencies of typically 50% or even lower accordingly limit external responsivities and quantum efficiencies.

The outstanding enhancement of the 3-dB bandwidth was achieved by a novel construction in which a vertically aligned germanium fin is sandwiched between two complementary in situ-doped silicon regions. Ion implantation can be waived completely, so unintended ion implantation into the light-sensitive germanium is avoided, which is very beneficial for high-speed performance, as minority-carrier diffusion effects are suppressed. The initial fabrication steps for our novel ultra-fast photodiodes are analogous to those of our previous photodetector generation process, which is part of IHP's ePIC (electronic photonic integrated circuit) technology 'SG25H5ePIC'^{16,19}. The selective epitaxial growth remains unchanged, including the thickness of the germanium body and the subsequent encapsulation in a thin Si layer. All processes for the separate depositions of the complementary in situ-doped silicon layers were conducted above the thick isolator stack. Accordingly, we do not expect substantial interference with underlying encapsulated devices such as modulators or transistors and believe that the integration into PIC or ePIC processes should be feasible.

Our ultra-fast germanium photodetectors pave the way for silicon photonics-based receivers for applications with symbol rates of 400 GBd or even beyond. Fabrication was entirely conducted on IHP's 8-inch BiCMOS pilot line facilities, so our approach proves that the conventional silicon technology available for standard 200-mm or 300-mm silicon substrates can match or even outperform InP technology in terms of high-speed waveguide-coupled photodetector performance, without the need to resort to more cumbersome III-V material transfer approaches. We demonstrate ultra-high 3-dB bandwidths and internal bandwidth-efficiency products, demonstrating the excellent performance of these germanium photodiodes as advanced waveguide-coupled photodetectors.

Online content

Any methods, additional references, Nature Research reporting summaries, source data, extended data, supplementary information, acknowledgements, peer review information; details of author contributions and competing interests; and statements of data and code availability are available at <https://doi.org/10.1038/s41566-021-00893-w>.

Received: 28 May 2021; Accepted: 14 September 2021;
Published online: 18 November 2021

References

- Wun, J.-M., Wang, Y.-W. & Shi, J.-W. Ultrafast uni-traveling carrier photodiodes with $\text{GaAs}_{0.5}\text{Sb}_{0.5}/\text{In}_{0.55}\text{Ga}_{0.47}\text{As}$ type-II hybrid absorbers for high-power operation at THz frequencies. *IEEE J. Select. Topics Quantum Electron.* **24**, 1–7 (2018).
- Dulme, S. et al. 300-GHz photonic self-mixing imaging-system with vertical illuminated triple-transit-region photodiode terahertz emitters. In *Proc. 2019 International Topical Meeting on Microwave Photonics (MWP)* 1–4 (IEEE, 2019); <https://doi.org/10.1109/MWP.2019.8892098>
- Rouvalis, E. et al. 170-GHz uni-traveling carrier photodiodes for InP-based photonic integrated circuits. *Opt. Express* **20**, 20090–20095 (2012).
- Rakowski, M. et al. 45-nm CMOS—silicon photonics monolithic technology (45CLO) for next-generation, low power and high speed optical interconnects. In *Proc. 2020 Optical Fiber Communications Conference and Exhibition (OFC)* 1–3 (IEEE, 2020).
- Boeuf, F. et al. A silicon photonics technology for 400-Gbit/s applications. In *Proc. 2019 IEEE International Electron Devices Meeting (IEDM)* 33.1.1–33.1.4 (IEEE, 2019).
- Knoll, D. et al. High-performance photonic BiCMOS process for the fabrication of high-bandwidth electronic-photonic integrated circuits. In *Proc. 2015 IEEE International Electron Devices Meeting (IEDM)* 15.6.1–15.6.4 (IEEE, 2015).
- Zhu, D. et al. A high performance Ge PIN photodiode compatible with high volume silicon photonics production processes. In *Proc. 2018 IEEE 15th International Conference on Group IV Photonics (GFP)* 1–2 (IEEE, 2018); <https://doi.org/10.1109/GROUP4.2018.8478742>
- Vivien, L. et al. Zero-bias 40-Gbit/s germanium waveguide photodetector on silicon. *Opt. Express* **20**, 1096–1101 (2012).
- Yu, F., Sun, K., Yu, Q. & Beling, A. Zero-bias high-speed evanescently coupled waveguide type-II UTC photodiode. In *Proc. 2020 Optical Fiber Communications Conference and Exhibition (OFC)* 1–3 (IEEE, 2020).
- Lischke, S. et al. Ge photodiode with -3-dB OE bandwidth of 110 GHz for PIC and ePIC platforms. In *Proc. 2020 IEEE International Electron Devices Meeting (IEDM)* 7.3.1–7.3.4 (IEEE, 2020).
- Colace, L. & Assanto, G. Germanium on silicon for near-infrared light sensing. *IEEE Photon. J.* **1**, 69–79 (2009).
- Lischke, S. et al. High bandwidth, high responsivity waveguide-coupled germanium p-i-n photodiode. *Opt. Express* **23**, 27213–27220 (2015).
- Shi, Y., Zhou, D., Yu, Y. & Zhang, X. 80-GHz germanium waveguide photodiode enabled by parasitic parameter engineering. *Photon. Res.* **9**, 605–609 (2021).
- Virot, L. et al. Integrated waveguide PIN photodiodes exploiting lateral Si/Ge/Si heterojunction. *Opt. Express* **25**, 19487–19496 (2017).
- Chen, H. et al. -1-V bias 67-GHz bandwidth Si-contacted germanium waveguide p-i-n photodetector for optical links at 56 Gbps and beyond. *Opt. Express* **24**, 4622–4631 (2016).
- Kato, K. Ultrawide-band/high-frequency photodetectors. *IEEE Trans. Microwave Theory Techn.* **47**, 1265–1281 (1999).

17. Picard, M.-J. et al. Novel spot-size converter for optical fiber to sub- μm silicon waveguide coupling with low loss, low wavelength dependence and high tolerance to alignment. In *Proc. 2015 European Conference on Optical Communication (ECOC 2015)* 1–3 (IEEE, 2015); <https://doi.org/10.1109/ECOC.2015.7341650>
18. Kato, K. et al. 110-GHz, 50%-efficiency mushroom-mesa waveguide p-i-n photodiode for a 1.55- μm wavelength. *IEEE Photon. Technol. Lett.* **6**, 719–721 (1994).
19. Lischke, S., Knoll, D., Mai, C. & Zimmermann, L. Advanced photonic BiCMOS technology with high-performance Ge photo detectors. In *Optical Sensing, Imaging and Photon Counting: from X-Rays to THz 2019* (ed. Mitrofanov, O.) (SPIE, 2019); <https://doi.org/10.1117/12.2530143>
20. Beling, A., Bach, H.-G., Mekonnen, G. G., Kunkel, R. & Schmidt, D. High-speed miniaturized photodiode and parallel-fed traveling-wave photodetectors based on InP. *IEEE J. Select. Topics Quantum Electron.* **13**, 15–21 (2007).
21. Runge, P., Zhou, G., Ganzer, F., Mutschall, S. & Seeger, A. Waveguide integrated InP-based photodetector for 100-Gbaud applications operating at wavelengths of 1,310 nm and 1,550 nm. In *Proc. 2015 European Conference on Optical Communication (ECOC)* 1–3 (IEEE, 2015).
22. Ma, P. et al. Plasmonically enhanced graphene photodetector featuring 100-Gbit/s data reception, high responsivity and compact size. *ACS Photonics* **6**, 154–161 (2019), <https://doi.org/10.1021/acspophotonics.8b01234>

Publisher's note Springer Nature remains neutral with regard to jurisdictional claims in published maps and institutional affiliations.



Open Access This article is licensed under a Creative Commons Attribution 4.0 International License, which permits use, sharing, adaptation, distribution and reproduction in any medium or format, as long as you give appropriate credit to the original author(s) and the source, provide a link to the Creative Commons license, and indicate if changes were made. The images or other third party material in this article are included in the article's Creative Commons license, unless indicated otherwise in a credit line to the material. If material is not included in the article's Creative Commons license and your intended use is not permitted by statutory regulation or exceeds the permitted use, you will need to obtain permission directly from the copyright holder. To view a copy of this license, visit <http://creativecommons.org/licenses/by/4.0/>.

© The Author(s) 2021, corrected publication 2021

Methods

Fabrication. Fabrication of our novel photodetectors was conducted on 8-inch SOI substrates with a buried oxide thickness of $2\text{ }\mu\text{m}$ and a top silicon layer of 220 nm . Nanowaveguides were realized through standard deep ultraviolet (DUV) lithography (248 nm), silicon-nitride hard-mask opening and a silicon dry etch. After overfilling with SiO_2 , the topography was removed by chemical-mechanical planarization (CMP), similar to common shallow-trench processes. The silicon-nitride hard mask serves as a stopping layer for the CMP and was subsequently removed. We applied another DUV lithography process to realize uniform 1D grating couplers using a silicon dry etch.

Deposition of a SiO_2 layer of a few hundreds of nanometres and subsequent planarization was the starting point for the germanium photodetector fabrication. Using I-line lithography and a SiO_2 dry etch, we realized windows in the thick oxide layer so that the silicon waveguides were locally exposed.

Similar to the process applied for manufacture of our previous germanium photodiodes^{6,12}, by selective epitaxial growth, germanium was deposited solely in the exposed windows, the regions where the photodiode was to be created. Subsequently, we entirely covered the germanium with a silicon layer using a non-selective epitaxial process. For both epitaxy processes we used a remote plasma chemical vapour deposition (RPCVD) system. Germanium was initially deposited at 300°C to obtain a 2D seed layer, followed by a germanium deposition at 550°C , followed by a cyclic post-anneal at 800°C . A silicon layer encapsulating the germanium was deposited over the entire wafer on top of the thick SiO_2 layer. This layer was removed by CMP such that silicon only remained in the actual photodiode region. Hard-mask deposition (SiO_2) was performed, then opening of the oxide by DUV lithography and dry etching of the germanium as described in Fig. 1a–d to form trenches and vertical sidewalls at one side of the germanium body. Non-selective epitaxy of in situ-doped silicon was then carried out. The remaining trench was overfilled with SiO_2 and the topography was removed again by CMP, leaving a planar surface free of silicon. The same process steps were conducted again to realize the complementary in situ-doped silicon layer alongside the germanium body. After removal of the silicon layer deposited on the second side of the photodiode, silicon offshoots were exposed such that silicide could be formed. The actual width of the realized germanium fin is defined by the relative positioning of the two DUV masks (for the p and n sides of the diode) and is thus not limited by the resolution of the deployed DUV tool.

Owing to the hardware limitations of our epitaxy tool, the doping concentrations of the in situ phosphorus layers (maximum concentration of $\sim 1\text{--}2 \times 10^{19}\text{ cm}^{-3}$) are somewhat lower than those of arsenic-doped layers (maximum concentration of $\sim 1 \times 10^{20}\text{ cm}^{-3}$; boron concentration is $\sim 1 \times 10^{20}\text{ cm}^{-3}$ as well). Compared to phosphorus, arsenic shows significantly more out-diffusion into the germanium, which is highly undesirable because of minority-carrier diffusion effects. Because the non-selective epitaxial growth of the in situ-doped layers is carried out at $\sim 700^\circ\text{C}$, the interface between the silicon and germanium will most probably be somewhat smeared. At such temperatures the diffusion of boron, arsenic and phosphorous in silicon can be neglected, but arsenic and phosphorous are known to diffuse more rapidly in germanium. We therefore developed a new process in which we introduce a dopant gradient in the phosphorus-doped silicon layer in close approximation to the germanium so as to reduce out-diffusion of phosphorous into the germanium. The total thickness of the phosphorous-doped silicon layer is only some tens of nanometres. On top of that layer, we also deposit an in situ arsenic-doped silicon layer by non-selective epitaxial growth. Furthermore, we replaced the cobalt-disilicide process that was used in ref.¹⁰ with a nickel-based process, which allowed for a significant reduction of the thermal budget²³. With these measures we could reduce dopant out-diffusion (which we could confirm by C–V measurements) into the germanium as well as decrease the resistance of the n-side of our photodiode, given the five to ten times higher doping concentration of in situ arsenic-doped layers with respect to phosphorous-doped ones.

After formation of the germanium fin and deposition of the in situ-doped silicon layers and their removal outside the actual photodetector region, a commonly used AlCu back end-of-line scheme was applied, with the formation of tungsten plugs and (several) metal layer(s).

Our fabrication process requires four mask steps for the photodiode itself (epitaxial window, opening of the p-side, opening of the n-side and exposure of the silicon offshoots) and another four masks for fabrication of silicon nanowaveguides, grating couplers, tungsten contacts and metal layer(s).

(Opto-)electrical S-parameter measurements. The LCA system (Keysight N4373D and N5227A) was used to measure the S_{21} frequency response of the photodiode. The measurements were performed in a range from 100 MHz to 67 GHz in 50 MHz steps. The excitation wavelength of the modulated signal from the LCA was $1,550\text{ nm}$ and was amplified to the desired optical power using the automated level control mode of the EDFA. A manual polarization controller was used to optimize the polarization. Reverse bias voltages of 0 V , 0.25 V , 0.5 V , 1 V and 2 V were supplied by source/measure unit (Keysight B2912A) through the PNA's integrated bias-tee and radiofrequency probe (FormFactor, GSG infinity probe). The characteristics were obtained with eightfold averaging and smoothing applied. S-parameter calibration was performed with the impedance standard substrate

ISS Cascade 101–190C. Open-short de-embedding was applied to account for the on-chip wiring. The chuck temperature of the wafer prober (Cascade AP300) was set to 27°C .

The network analyser (Keysight PNA N5227A) was also used to measure the reflection characteristics (S_{21}) of the photodiode in a frequency domain from 100 MHz to 67 GHz . The radiofrequency power was set to -30 dBm and fourfold averaging was applied. Open-short de-embedding was applied to account for the on-chip wiring. The capacitance of the photodiode was extracted from S_{21} values averaged around 30 GHz for bias voltages in a range from 0.3 V to -2 V . The chuck temperature of the wafer prober (Cascade AP300) was set to 27°C .

Heterodyne radiofrequency measurements. Heterodyne measurements were performed using both coaxial and rectangular waveguide-based approaches for signal extraction, as shown in Supplementary Figs. 1 and 2, respectively. For each approach, two tunable external cavity lasers were used to generate the radiofrequency beat note, for which the modulation depth was maximized by matching both the lasers' polarization and output power. The signal was then split, with 1% going to an electrical spectrum analyser (d.c. to 50 GHz) and an optical wavelength meter ($>50\text{ GHz}$) and 99% going to an EDFA. A variable optical attenuator was used to control the amount of light incident on the photodiodes. A final polarization controller was used to optimize the light incident on the photodiode's grating coupler, which was coupled to the photodiode via a lightwave probe. From d.c. to 110 GHz , a 1.0-mm coaxial GSG probe was used to extract the radiofrequency beat note from the photodiode. The probe was connected to the d.c. + radiofrequency port of an external 110-GHz bias-tee, which was biased through the d.c. port from a source meter unit (SMU) and connected to a 1.0-mm 110-GHz Rohde & Schwarz thermal power sensor through the radiofrequency port. The radiofrequency power and optical signals were monitored on a computer. The probe loss was calibrated from the probe's data sheet, the coaxial cable and bias-tee link were calibrated with an S-parameter measurement generated from a network analyser, and the power meter was calibrated using a look-up table. Above 110 GHz , GSG WR-6, WR-5 and WR-3 rectangular waveguide probes from GGB were used to measure at $110\text{--}170\text{ GHz}$, $140\text{--}220\text{ GHz}$ and $220\text{--}325\text{ GHz}$, respectively. The probe loss was again calibrated from the data sheet, which included the loss incurred from the built-in bias-tee on each probe. Connecting each probe to a VDI PM5 power meter was a 1-inch WR-x to WR-10 tapered waveguide block, for which the calibration was taken from the data sheet. The PM5 power meter output was monitored on a computer. It should be noted that, although manufacturer calibration data are only provided up to 325 GHz , measurements were taken up to 350 GHz and are therefore shown as 'worst-case' uncalibrated above 325 GHz . Furthermore, factoring in radiofrequency loss, the noise floors for the 110-GHz and 325-GHz measurements were -31 dBm and -26.2 dBm , respectively.

To obtain the full frequency response as shown in Fig. 3, we first measured the frequency bands independently and overlapped those measurements, for example the $110\text{--}170\text{ GHz}$ overlaps with the higher bound of the d.c. to 110-GHz measurement, and overlaps with the lower bound of the $140\text{--}220\text{-GHz}$ measurement. We then calibrated each measurement band independently, as described above. The curves were finally plotted altogether. If their overlaps aligned well with the respective other measurement curves, we knew that each separate measurement curve and its respective calibration were fine.

D.c. electrical measurements. The $I\text{-}V$ characteristics were measured at wafer level on an automated 8-inch wafer prober (Cascade Microtech) with heatable chuck using a d.c.-analyser (Agilent 4156 precision semiconductor parameter analyser). Two SMUs are used to apply the bias (sweep) and ground to the pads of the photodiode, respectively. Probing was performed using standard d.c. probes (tungsten).

D.c. optical measurements. For estimation of the photodiode responsivity, the photocurrent was measured at different optical powers as a function of bias voltage. The silicon photonics testing platform established by FormFactor, based on a semi-automated wafer prober (CM300xi), and automated six-axis positioning stages (PI) were used. A tunable laser source (Keysight 81608A) and SMU (Keysight B2912A) were used to perform measurements. The light from a cleaved single-mode fibre was coupled to the grating coupler using an automated fibre alignment routine. The polarization was manually optimized. The excitation wavelength was set to $1,550\text{ nm}$ and the power, measured at the fibre tip, was swept from -1 dBm to 8 dBm in steps of 1 dB . The characteristics of photocurrent versus applied voltage in the range from 0.3 V to -2 V in steps of 0.1 V were obtained. D.c. probing was performed by a standard ground-signal (GS) probe. The quotient of the photocurrent and the optical power (at the fibre tip) at the desired voltage gave the value of external responsivity. Reducing the optical power by subtracting the loss of the grating coupler gave the internal responsivity. The chuck temperature of the wafer prober was set to 27°C .

The equipment used for characterization of photocurrents is regularly used for process control measurements in our foundry. We expect the uncertainty in these measurements to be 1 dB or less (in other words $\pm 0.5\text{ dB}$), such that the actual coupling losses would lie between 3.5 dB and 4.5 dB per grating coupler, which

equates to efficiencies of 45% to 35%. Hence, a measurement uncertainty of 1 dB would lead to change of $\pm 5\%$ in the photocurrent and thus in the responsivity as well.

Data availability

The data that support the findings of this study are available from the corresponding author upon reasonable request.

References

23. Lischke, S. et al. High-speed, high-responsivity Ge photodiode with NiSi contacts for an advanced photonic BiCMOS technology. In *2017 IEEE 14th International Conference on Group IV Photonics (GFP)* 61–62 (IEEE, 2017).

Acknowledgements

We gratefully acknowledge support from IHP colleagues J. Katzer and M. A. Schubert for the preparation of the lamella by focused ion beam, as well as the STEM images, D. Wolansky for support and processing of nickel silicide, D. Schmidt and A. Kroh for extensive electrical characterization, O. Fursenko for ellipsometry measurements and A. Trusch as representative of IHP's entire cleanroom team. We also acknowledge funding by the German Ministry of Research and Education (BMBF), project PEARLS (grant no. 13N14936), support of the German Research Foundation (DFG) project EPIDAC (grant

no. ZI1283-7-1) as well as support by the European Commission, project plaCMOS (grant ID 780997).

Author contributions

S.L. designed and fabricated the photodiodes and wrote the manuscript with contributions from all authors. A.P., J.S.M., K.S. and F.K. performed extensive optoelectrical characterization, and Y.Y. grew the germanium as well as the in situ-doped silicon layers. M.F. and S.M. developed and conducted the dry etch processes. A.K. performed CMP processes. C.M. created layouts for the devices and test structures. S.L., D.S., A.B. and L.Z. analysed the results.

Competing interests

The authors declare no competing interests.

Additional information

Supplementary information The online version contains supplementary material available at <https://doi.org/10.1038/s41566-021-00893-w>.

Correspondence and requests for materials should be addressed to S. Lischke.

Peer review information *Nature Photonics* thanks Leopold Virot and the other, anonymous, reviewer(s) for their contribution to the peer review of this work.

Reprints and permissions information is available at www.nature.com/reprints.